Ceramics International 45 (2019) 5218–5222

Contents lists available at ScienceDirect

Ceramics International

journal homepage: www.elsevier.com/locate/ceramint

Sintering evaluation of doped lanthanum gallate based on thermodilatometry

R.M. Batista, S.L. Reis*, R. Muccillo, E.N.S. Muccillo

Energy and Nuclear Research Institute - IPEN, PO Box 11049, S. Paulo 05422-970, SP, Brazil

ARTICLE INFO

Keywords:
A. Powders: solid state reaction
A. Sintering
D. Perovskites
E. Fuel cells

ABSTRACT

The sintering behavior of $La_{0.9}Sr_{0.1}Ga_{0.8}Mg_{0.2}O_{3-\delta}$ oxide-ion conductor was systematically investigated by thermodilatometry. The shrinkage data obtained with heating rates of 4, 7, 10 and 12 °C min^{-1} were analyzed by the constant rate of heating model and by construction of the master sintering curve. Validation of the master sintering curve was carried out by measurements of density in conventionally sintered specimens. Slight anisotropy of shrinkage data was found and changes to the basic equation of density was proposed to account for this effect. Plotting the data determined by the constant rate of heating model versus density allowed an easy identification of the density range of constant activation energy. The activation energy (865 kJ mol^{-1}) obtained from the master sintering curve correlates quite well with that (874 kJ mol^{-1}) obtained by the constant rate of heating model.

1. Introduction

Nowadays there is a growing demand on advanced ceramic materials with suitable properties for technological applications in diverse areas such as energy, sensors and microelectronics. The manufacturing processes of these ceramics should be able to produce solid pieces with required dimensions and physical properties [1].

In spite of recent developed technologies for fabrication of ceramic components, the most utilized manufacturing processes still encompass several steps, the sintering step being essential for obtaining the final properties.

Sintering is a thermodynamic process where several phenomena take place simultaneously at microscopic level, promoting continuous changes of the microstructure [2,3]. Close control of the sintering process is often required owing to the relationship between microstructure features and physical properties.

Theoretical and experimental approaches have been used to control the sintering process with emphasis in multi-scale simulation methodologies [4,5] and new experimental methods [6–9]. A recent comprehensive review on sintering mechanisms and models may be found in [10].

Two methodologies based on linear shrinkage data have been extensively used to exploit the sintering process of ceramic powder compacts: the constant rate of heating (CRH) model [11] and the construction of the master sintering curve (MSC) [12]. Particularly, the MSC approach has been successfully applied to investigate the microstructure characteristics of several ceramic systems sintered under arbitrary profiles of temperature and time [13–16]. At first, that methodology was proposed to predict the density evolution of a ceramic compact during sintering. In the last two decades, the MSC approach has been extended to account for different sintering methods and to investigate sintering kinetics [17,18]. Recently, the MSC methodology has been applied to more complex ceramic and metal systems such as ceramic-ceramic composites [19], dual-phase stainless steel [20] and functionally graded ZnO ceramics [21]. However, the sintering process of relatively few oxide-ion conductors has been investigated so far, with emphasis on fluorite-type oxides such as stabilized zirconia and doped ceria [17,18,22–26].

Oxide-ion conductors based on lanthanum gallate with partial substitutions for strontium and magnesium in the A- and B-sites, respectively, of the perovskite structure are considered promising candidates for application in solid oxide fuel cells operating at intermediate temperatures (500–700 °C), due to their electrical and electrochemical properties [27,28]. Sintering of these solid electrolytes is usually performed at high temperatures (higher than 1400 °C) yielding impurity phases. Then, the design of sintering cycles able to decrease the sintering time and/or temperature with consequent reduction of the grain growth is highly advantageous and somehow desirable to minimize production costs.

In this work, two methodologies were applied to evaluate the

* Corresponding author.
E-mail address: shirley.reis@usp.br (S.L. Reis).

https://doi.org/10.1016/j.ceramint.2018.11.217
Received 4 July 2018; Received in revised form 11 October 2018; Accepted 26 November 2018
Available online 28 November 2018
0272-8842/

sintering process of doped lanthanum gallate, aiming to predict the evolution of density and to determine the apparent activation energy for sintering: the CRH model and the construction of the MSC.

2. Experimental

The $La_{0.9}Sr_{0.1}Ga_{0.8}Mg_{0.2}O_{3-\delta}$ (hereafter LSGM) nominal composition was prepared from the stoichiometric mixture of La_2O_3 (99.9%), Ga_2O_3 (99.99%), $SrCO_3$ (P.A.) and MgO (P.A.) by the solid-state reaction method. In brief, the process consists of three steps of calcination at 1250 °C for 4 h with intermediate deagglomeration in agate mortar with pestle. After calcination the powder is subjected to attrition milling for 1 h with isopropyl alcohol and then dried in an oven at 40 °C. A detailed description of this method and specific parameters may be found elsewhere [29].

Green compacts with 6 mm diameter and 5 mm thickness were prepared by uniaxial (50 MPa) followed by cold isostatic pressing at 100 MPa (National Forge Co) for thermodilatometry (or dilatometry) experiments. For conventional sintering, specimens with 8 mm diameter and 2 mm thickness were prepared according to the same procedure.

Conventional sintering was performed in a resistive furnace (Lindberg BlueM) in the 1000–1500 °C range with holding times from null to 12 h and heating rate of 10 °C min^{-1}.

Thermodilatometry experiments were carried out in a vertical push-rod type dilatometer (Anter, Unitherm™ 1161) with nominal precision of 1 μm. The compacts were heated with 4, 7, 10 and 12 °C min^{-1} heating rates up to 1500 °C and therefore cooled down at 10 °C min^{-1} to room temperature. These experiments were performed in duplicate for reproducibility purpose.

The sintered density was determined by the water immersion method and compared to the theoretical density. Structural characterization was carried out by X-ray diffraction (XRD) measurements (Bruker-AXS, D8 Advance) in the $20° \leq 2\theta \leq 80°$ range with Ni-filtered Cu K_α radiation ($\lambda = 1.5405$ Å). Rietveld refinement of the XRD pattern was carried out using (General Structure Analysis System) GSAS [30]. Correction for instrumental broadening was accomplished by measuring a cerium dioxide standard. The predominant structure of this compound was indexed according to (Inorganic Crystal Structure Database) ICSD # 51-288 file with orthorhombic symmetry.

The mean grain size was estimated by the intercept method on scanning electron microscopy (FEI Inspect - F50) micrographs.

The experimental data obtained by thermodilatometry were analyzed by the CRH method as modified by Wang and Raj [31]. The MSC was constructed by calculating the work of sintering [12] assuming a sigmoid function. Corrections applied to dilatometry data were due to thermal expansion of the probe and specimen, as proposed in [32]. The former was obtained by measuring a translucent alumina (Crystallox®). The thermal expansion coefficient was determined from the slope of the shrinkage straight line recorded in the cooling process.

The CRH and the MSC methodologies are based on the combined-stage sintering model [33]. In brief, in this model the rate of densification of an isotropic specimen during sintering is described by:

$$-\frac{dL}{Ldt} = \frac{d\rho}{3\rho dt} = \frac{\gamma\Omega}{kT}\left(\frac{\delta D_{gb}\Gamma_{gb}}{G^4} + \frac{D_v\Gamma_v}{G^3}\right) \quad (1)$$

where L is the specimen length, t the time, ρ the density, T the absolute temperature, k the Boltzmann constant, γ the surface energy, Ω the atomic volume, δ the thickness of grain boundaries, G the mean grain size, D_i the diffusion coefficients, and Γ_i the lumped scaling parameters, with $i = gb, v$. The subscripts gb and v stand for grain boundary and volume, respectively, and are related to diffusion mechanisms. The lumped scaling parameters contain density-dependent geometric terms. The diffusion coefficients are defined by the usual Arrhenius expression with D_{0i} and Q_i being the pre-exponential factor and the activation energy, respectively.

Assuming that a single densification mechanism predominates, Eq. (1) may be rewritten as:

$$\ln\left(\frac{T}{\rho}\frac{d\rho}{dt}\right) = \ln\left(\frac{3\gamma\Omega}{kT}\frac{D_{0v}\Gamma_v}{G^3}\right) - \frac{Q_v}{kT} \quad (2)$$

In addition, if the mean grain size depends only on the density, the first term in the right-hand side of Eq. (2) becomes just a function of density.

In this derivation only volume diffusion was taken into account. Similar equation may be written for the boundary diffusion mechanism.

Construction of the MSC involves similar hypothesis than those for the CRH method. In this case, Eq. (1) is simplified and rearranged separating the microstructure terms from those depending on the thermal history, such that [12]:

$$\int_0^t \frac{1}{T}\exp\left(-\frac{Q}{RT}\right)dt = \frac{k}{\gamma\Omega D_0}\int_{\rho_0}^{\rho}\frac{(G(\rho))^3}{3\rho\Gamma_v(\rho)}d\rho \quad (3)$$

where R is the gas constant. The right-hand side of Eq. (3) contains all terms related to the microstructure, and the left-hand side term depends simply on the temperature-time profile and the activation energy of the mass transport mechanism. Then, the work of sintering, $\Theta(t, T(t))$, representing a measure of the energy supplied to the compact during non-isothermal sintering, is defined as [12]:

$$\Theta(t, T(t)) = \int_0^t \frac{1}{T}\exp\left(-\frac{Q}{RT}\right)dt \quad (4)$$

In this case, the analysis of the sintering process of LSGM was carried out by applying Eqs. (2) and (4) using a software specially developed for that purpose [34].

3. Results and discussion

Fig. 1 shows the room temperature XRD pattern of LSGM specimen sintered at 1350 °C for 2 h. The Rietveld refinement provided good fitting of this pattern with low value of χ^2 (1.86). The diffraction peaks were indexed according to the orthorhombic symmetry (ICSD 51-288). A small amount (~5%) of $LaSrGa_3O_7$ (indicated by * in the diffraction profile) was estimated from pattern refinement.

The lattice parameters a, b and c of the distorted orthorhombic structure (space group *Imma*) and the theoretical density of $La_{0.9}Sr_{0.1}Ga_{0.8}Mg_{0.2}O_{3-\delta}$ obtained from pattern refinement are summarized in Table 1. Those figures are in good agreement with previous reported values [35].

The high temperature range of linear shrinkage curves of LSGM

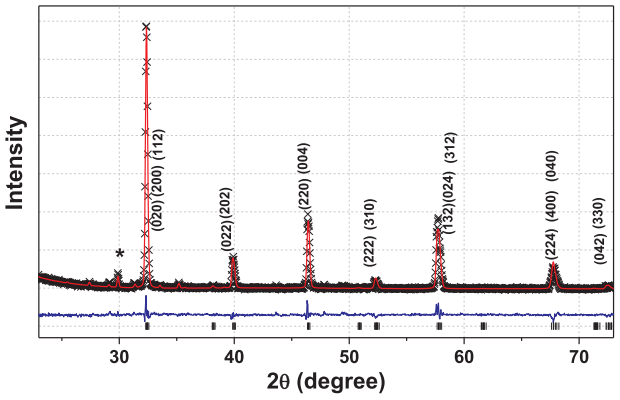

Fig. 1. XRD pattern of LSGM specimen sintered at 1350 °C for 2 h and data from Rietveld refinement. Crosses = experimental data, solid (red) = calculated, solid (blue) at bottom = difference and tick mark = Bragg position. (For interpretation of the references to color in this figure, the reader is referred to the web version of this article)

Table 1
Values of lattice parameters a, b and c, and theoretical density of the orthorhombic phase of LSGM determined by XRD pattern refinement.

Parameters	Values
a (Å)	5.5056(9)
b (Å)	7.8241(7)
c (Å)	5.5387(5)
Theoretical density (g cm^{-3})	6.682

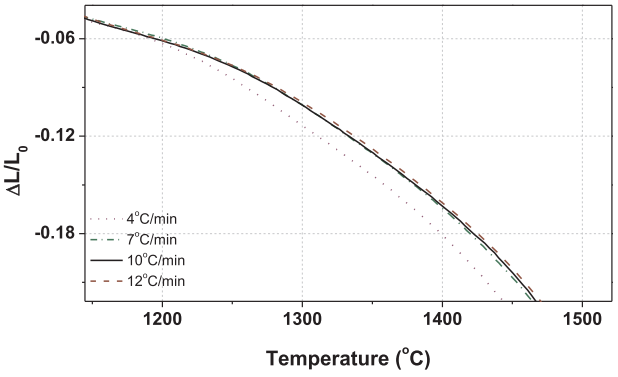

Fig. 2. High-temperature range of linear shrinkage curves of LSGM compacts obtained under several heating rates.

compacts recorded with several heating rates is depicted in Fig. 2.

The evolution of the linear shrinkage is similar for all curves. The one registered with the slowest heating rate exhibited faster shrinkage than the others, as previously noted for other materials [12,14]. This effect is attributed to the large amount of thermal energy transferred to the compact heated at low heating rates. The maximum shrinkage rate (−0.012%/°C) occurs at 1460 °C evidencing the low sinterability of LSGM prepared by the solid-state method. The average coefficient of thermal expansion of LSGM determined in the 400–1400 °C range is 9.7×10^{-6} °C^{-1}.

The LSGM compacts utilized for thermodilatometry experiments achieved 96–98% of relative density and about 2 μm of mean grain size, as shown in Fig. 3. In addition, the compacts exhibited negligible (< 2%) weight loss and differential shrinkage. Table 2 list values of shrinkage determined in the axial and radial directions of LSGM compacts obtained under several heating rates.

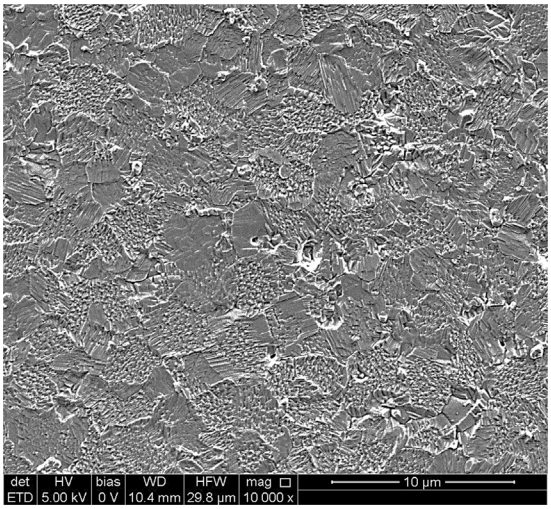

Fig. 3. Scanning electron microscope micrograph of the LSGM compact heated at a rate of 4 °C min^{-1}.

Table 2
Values of axial and radial shrinkages of LSGM compacts heated at several rates.

Heating rate (°C min^{-1})	Axial	Radial
4	−0.2486	−0.2240
7	−0.2553	−0.2215
10	−0.2544	−0.2231
12	−0.2679	−0.2267

The axial shrinkage is slightly higher than the radial one (Table 2). In addition, the radial shrinkage exhibits similar values independent on the heating rate (within experimental errors). The same behavior holds for the axial shrinkage. It is well-known that LSGM is not single phase material when prepared by solid state reaction. The distribution of impurity phases ($LaSrGa_3O_7$, $La_4Ga_2O_9$, $LaSrO_4$ and MgO) is assumed to be random, but there are preferred positions. MgO, for example is usually found as a precipitated phase along the grain boundaries [29]. These impurity phases behave distinctly during sintering and may account for the slight difference observed between the radial and axial shrinkages.

Then, this slight anisotropic shrinkage behavior seems to be an intrinsic characteristic of LSGM, owing to its complex composition with simultaneous diffusion of several cations (La, Sr, Ga and Mg) during sintering. This anisotropic shrinkage imposed a change of the usual density (ρ) equation to:

$$\rho = \frac{\rho_0}{\left(1+\frac{\Delta L}{L_0}\right).\left(1+k\frac{\Delta L}{L_0}\right).\left(1+k\frac{\Delta L}{L_0}\right)} \quad (5)$$

where ρ_0, L_0 and ΔL are the green density, the initial length and the difference between the instantaneous and the initial length of the compact; k is a proportionality constant obtained from the radial to axial shrinkage ratio.

Fig. 4 shows the density curves calculated from linear shrinkage data applying Eq. (5).

The density evolution may be separated into three steps. The first, from room temperature up to ~1000 °C is characterized by insignificant increment on density (~2%). The second, from ~1000 to ~1300 °C exhibits a gradual, but modest densification (13%). The last step, for temperatures beyond ~1300 °C, is dominated by a fast increase of density. Indeed, the LSGM specimen sintered at 1300 °C for 2 h that was utilized for XRD experiment (Fig. 1) attained 92% of relative density. Then, for temperatures higher than 1300 °C, grain growth and consequent speed up of densification of LSGM are expected to occur. Similar behavior of the linear shrinkage was observed in chemically synthesized LSGM [36].

The density curves (Fig. 4) were used to construct the MSC of LSGM in the whole density range (45–98%), Fig. 5. The inset shows the typical dependence of the mean residual squares on activation energy (Q)

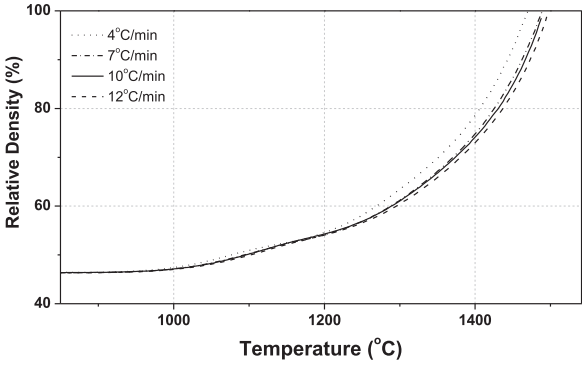

Fig. 4. High-temperature range of density curves of LSGM compacts obtained under several heating rates applying Eq. (5). (See text for details).

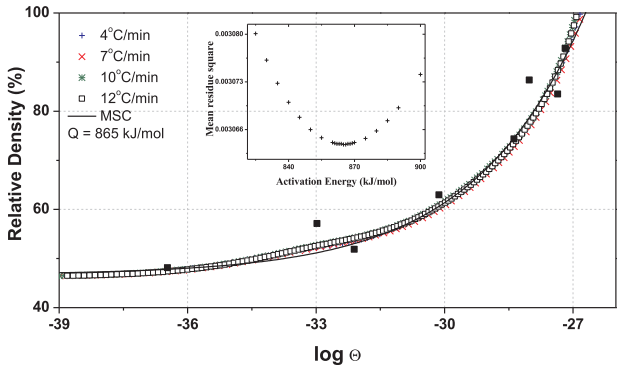

Fig. 5. Convergence of density data (symbols) obtained for LSGM compacts sintered under several heating rates and the corresponding MSC (solid line). Discrete points are density values determined for conventionally (isothermal and non-isothermal) sintered specimens. Inset: mean residual squares versus activation energy.

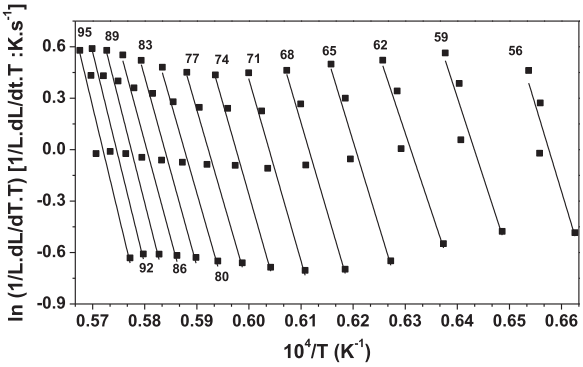

Fig. 6. Arrhenius plots of LSGM for estimate the activation energy for sintering according to the CRH method. Numbers stand for relative density (in %).

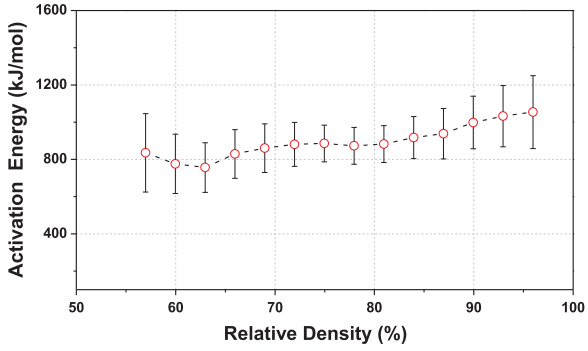

Fig. 7. Evolution of the apparent activation energy for sintering LSGM determined by the CRH method.

values. Minimization of the mean residual squares was obtained for Q = 865 kJ mol^{-1}.

The experimental data (symbols) obtained with several heating rates, shown in Fig. 5, exhibit good conversion and good fitting with the MSC (line) in the wide range of *log*Θ investigated. The validation of the MSC was obtained from density values determined for LSGM specimens sintered isothermally and non-isothermally by the conventional method (discrete points). These results support the proposed correction to take into account the slight anisotropic behavior of LSGM.

In order to further evaluate the reliability of the apparent activation energy for sintering determined from the MSC methodology, the CRH model was applied to the same data set. Fig. 6 shows Arrhenius plots of the sintering data in the 56–95% relative density range.

In this case, the apparent activation energy at a given density was determined from the slope of the least square fit of the sintering data for the specific relative density. The straight lines are parallel to each other in the ~68 to ~82% relative density range. At high and low relative densities, different slopes are observed. Changes of slope in Arrhenius plots of simple oxides are usually associated to several factors, such as bi-or multimodal distribution of particle sizes of the starting powder, changes in the rate-determining mechanism of sintering or even in the relative weight of competing mechanisms [11].

Values of the apparent activation energy for sintering calculated from Arrhenius plots versus density are depicted in Fig. 7.

The average value of the activation energy for sintering in the 68–82% relative density range amounts 874 kJ mol^{-1}, which is close to that determined by the MSC analysis. Then, it may be concluded that in the second stage of sintering (corresponding roughly to the 68–82% relative density range), there is no change in the rate-controlling mechanism of LSGM. The relatively large standard deviation (± 100 kJ mol^{-1}) of the activation energy in Fig. 7 may be a consequence of the simultaneous diffusion of the four cations in this complex oxide.

4. Conclusions

The sintering process of $La_{0.9}Sr_{0.1}Ga_{0.8}Mg_{0.2}O_{3-\delta}$ oxide-ion conductor prepared by solid-state synthesis was investigated by thermodilatometry. Data analysis was conducted by the constant rate of heating model and by construction of the master sintering curve. The slight anisotropy of the shrinkage data was treated by changing the basic density equation. Validation of the master sintering curve was accomplished by density measurements of conventionally sintered specimens. The value of the activation energy for sintering obtained from the master sintering curve (865 kJ mol^{-1}) is close to that determined by the constant rate of heating model (874 kJ mol^{-1}) in the second stage of sintering.

Acknowledgements

The authors acknowledge FAPESP (2013/07296-2), CNPq (304073/2014-8) and CNEN for financial supports.

References

[1] R.M. German, Sintering: From the Empirical Observations to Scientific Principles, Butterworth-Heinemann, Oxford, 2014 (ISBN: 9780124016774).
[2] W.D. Kingery, H.K. Bowen, D.R. Uhlmann, Introduction to Ceramics, 2nd ed., Wiley, New York, 1968 (ISBN: 978-0471478607).
[3] M.N. Rahaman, Ceramic Processing and Sintering, 2nd ed, CRC Press, New York, 1995 (ISBN: 9780824709884).
[4] E.A. Olevsky, Modeling of sintering: challenges and further development, in: A. Lawley, J. Smugeresky (Ed.), Proceedings of International Conference on Process Modeling in Powder Metallurgy and Particle Material, Newport-Beach, MPIF, 2002, pp. 27–33. (ISBN:1-55899-667-2).
[5] E.A. Olevsky, V. Tikare, T. Garino, Multi-scale study of sintering: a review, Am. J. Ceram. Soc. 89 (6) (2006) 1914–1922, https://doi.org/10.1111/j.1551-2916.2006.01054.x.
[6] D. Agrawal, Microwave sintering of ceramics, composites, and metal powders, in: Z.Z. Fang (Ed.), Sintering of Advanced Materials, 9 Woodhead, Cambridge, 2010, pp. 222–248 (ISBN: 978-1845695620).
[7] I. Wei-Chen, X.H. Wang, Sintering dense nanocrystalline ceramics without final-stage grain growth, Nature 404 (2000) 168–171, https://doi.org/10.1038/35004548.
[8] M. Cologna, B. Rashkova, R. Raj, Flash sintering of nanograin zirconia in < 5 s at 850 °C, J. Am. Ceram. Soc. 93 (2010) 3556–3559, https://doi.org/10.1111/j.1551-2916.2010.04089.x.
[9] F. Bouville, A.R. Studart, Geologically-inspired strong bulk ceramics made with water at room temperature, Nat. Commun. 8 (2017) 14655, https://doi.org/10.1038/ncomms14655.
[10] R.K. Bordia, S.-J.L. Kang, E.A. Olevsky, Current understanding and future research directions at the onset of the next century of sintering science and technology, J. Am. Ceram. Soc. 100 (2017) 2314–2352, https://doi.org/10.1111/jace.14919.
[11] W.S. Young, I.B. Cutler, Initial sintering with constant rates of heating, J. Am. Ceram. Soc. 53 (1970) 659–663, https://doi.org/10.1111/j.1151-2916.1970.tb12036.x.
[12] H. Su, D.L. Johnson, Master sintering curve: a practical approach to sintering, J.

Am. Ceram. Soc. 79 (1996) 3211–3217, https://doi.org/10.1111/j.1151-2916.1996.tb08097.x.
[13] T.R.G. Kutty, K.B. Khan, P.V. Hedge, J. Banerjee, A.K. Sengupta, S. Majumbar, H.S. Kamath, Development of a master sintering curve for ThO_2, J. Nucl. Mater. 327 (2004) 211–219, https://doi.org/10.1016/j.jnucmat.2004.02.007.
[14] K.G. Ewsuk, D.T. Ellerby, C.B. DiAntonio, Analysis of nanocrystalline and microcrystalline ZnO sintering using master sintering curves, J. Am. Ceram. Soc. 89 (2006) 2003–2009, https://doi.org/10.1111/j.1551-2916.2006.00990.x.
[15] W.-Q. Shao, S.-O. Chen, D. Li, H.-S. Cao, Y.-C. Zhang, X.-H. Ge, Prediction of densification during low heating rate sintering of microcrystalline alumina ceramics based on master sintering curve theory, Mater. Technol. 23 (2008) 19–22, https://doi.org/10.1179/175355508×266917.
[16] M. Mazaheri, A. Simchi, M. Dourandish, F. Golestani-Fard, Master sintering curves of s nanoscale 3Y-TZP powder compacts, Ceram. Int. 35 (2009) 547–554, https://doi.org/10.1016/j.ceramint.2008.01.008.
[17] V. Pouchly, K. Maca, Z. Shen, Two-stage master sintering curve applied to two-step sintering of oxide ceramics, J. Eur. Ceram. Soc. 33 (2013) 2275–2283, https://doi.org/10.1016/j.jeurceramsoc.2013.01.020.
[18] K. Rajeswari, S. Padhi, A.R.S. Reddy, R. Johnson, D. Das, Studies on sintering kinetics and correlation with the sinterability of 8Y zirconia ceramics based on the dilatometric shrinkage curves, Ceram. Int. 39 (2013) 4985–4990, https://doi.org/10.1016/j.ceramint.2012.11.095.
[19] A.J. Rayner, R.M.C. Clemmer, S.F. Corbin, Determination of the activation energy and master sintering curve for NiO/YSZ composite solid oxide fuel cell anodes, J. Am. Ceram. Soc. 98 (2015) 1060–1065, https://doi.org/10.1111/jace.13405.
[20] I.D. Jung, S. Ha, S.J. Park, D.C. Blaine, R. Bollina, R.M. German, Two-phase master sintering curve for 17-4 PH stainless steel, Metal. Mater. Trans. 47A (2016) 5548–5556, https://doi.org/10.1007/s11661-016-3687-0.
[21] C.R. Cramer, J. Gonzalez-Julian, P.S. Colasuonno, T.B. Holland, Continuous functionally graded material to improve the thermoelectric properties of ZnO, J. Eur. Ceram. Soc. 37 (2017) 4693–4700, https://doi.org/10.1016/j. jeurceramsoc.2017.07.019.
[22] X. Song, J. Lu, T. Zhang, J. Ma, Two-stage master sintering curve approach to sintering kinetics of undoped and Al_2O_3-doped 8 mol% yttria-stabilized cubic zirconia, J. Am. Ceram. Soc. 94 (2011) 1053–1059, https://doi.org/10.1111/j.1551-2916.2010.04199x.
[23] E. Jud, C.B. Huwiler, L.J. Gauckler, sintering analysis of undoped and cobalt oxide doped ceria solid solutions, J. Am. Ceram. Soc. 88 (2005) 3013–3019, https://doi.org/10.1111/j.1551-2916.2005.00567x.
[24] D.Z. De Florio, V. Esposito, E. Traversa, R. Muccillo, F.C. Fonseca, Master sintering curve for Gd-doped CeO_2 solid electrolytes, J. Therm. Anal. Calorim. 97 (2009) 143–147, https://doi.org/10.1007/s10973-009-0238-6.
[25] L. Guan, S. Le, S. He, X. Zhu, T. Liu, K. Sun, Densification behavior and space charge blocking effect of Bi_2O_3 and Gd_2O_3 co-doped CeO_2 as electrolyte for solid oxide fuel cells, Electrochim. Acta 161 (2015) 129–136, https://doi.org/10.1016/j.electacta.2015.02.090.
[26] R.M. Batista, E.N.S. Muccillo, Analysis of the sintering process in gadolinia-doped ceria by thermodilatometry and correlation with microstructure evolution, J. Therm. Anal. Calorim. 132 (2018) 851–867, https://doi.org/10.1007/s10973-018-6969-5.
[27] T. Ishihara, M. Honda, Y. Takita, Doped $LaGaO_3$ perovskite-type oxide as a new oxide ionic conductor, J. Am. Chem. Soc. 116 (1994) 3801–3803, https://doi.org/10.1021/ja00088a016.
[28] M. Feng, J.B. Goodenough, A superior oxide-ion electrolyte, Eur. J. Solid State Inorg. Chem. 31 (1994) 663–672.
[29] S.L. Reis, E.N.S. Muccillo, Preparation of dense $La_{0.9}Sr_{0.1}Ga_{0.8}Mg_{0.2}O_{3-\delta}$ with high ionic conductivity by solid-state synthesis, Ionics 24 (2018) 1693–1700, https://doi.org/10.1007/s11581-017-2344-y.
[30] A. C. Larson, R. B. von Deele, General structure analysis system (GSAS), Los Alamos National Laboratory Report, LAUR, 1994, pp. 86–748.
[31] J. Wang, R. Raj, Estimate of the activation energy for boundary diffusion from rate-controlled sintering of pure alumina and alumina doped with zirconia or titania, J. Am. Ceram. Soc. 73 (1990) 1172–1175, https://doi.org/10.1111/j.1151-2916.1990.tb05175.x.
[32] R.M. Batista, E.N.S. Muccillo, Dilatometry analysis of the sintering process of nanostructured gadolinia-doped ceria, J. Therm. Anal. Calorim. 126 (2016) 1007–1013, https://doi.org/10.1007/s10973-016-5674-5.
[33] J.D. Hansen, R.P. Rusin, M.-H. Teng, D.L. Johnson, Combined-stage sintering model, J. Am. Ceram. Soc. 75 (1992) 1129–1135, https://doi.org/10.1111/j.1151-2916.1992.tb05549.x.
[34] R.M. Batista, J.F.R. Naranjo, E.N.S. Muccillo, A versatile software for the construction of the master sintering curve, Mater. Sci. Forum 912 (2018) 240–244, https://doi.org/10.4028/www.scientific.net/MSF.912.240.
[35] M. Lerch, H. Boysen, T. Hansen, High-temperature neutron scattering investigation of pure and doped lanthanum gallate, J. Phys. Chem. Solids 62 (2001) 445–455, https://doi.org/10.1016/S0022-3697(00)00078-0.
[36] K. Traina, C. Henrist, B. Vertruyen, R. Cloots, Dense $La_{0.9}Sr_{0.1}Ga_{0.8}Mg_{0.2}O_{2.85}$ electrolyte for IT-SOFC's: sintering study and electrochemical characterization, J. Alloy. Compd. 509 (2011) 1493–1500, https://doi.org/10.1016/j.jallcom.2010.10.117.